



Defects rich g-C₃N₄ with mesoporous structure for efficient photocatalytic H₂ production under visible light irradiation

Daming Ruan, Sooyeon Kim, Mamoru Fujitsuka, Tetsuro Majima*

The Institute of Scientific and Industrial Research (SANKEN), Osaka University, Mihogaoka 8-1, Ibaraki, Osaka 567-0047, Japan

ARTICLE INFO

Keywords:

g-C₃N₄
Photocatalytic H₂ production
Visible light photocatalysis
Mesoporous structure with defects
Electron trapping

ABSTRACT

Graphitic carbon nitride (g-C₃N₄) is a promising visible-light-driven photocatalyst for solar energy conversion by splitting water into H₂. However, the photocatalytic performance of g-C₃N₄ is not sufficient because of low surface area and fast recombination of charge carriers. Here, g-C₃N₄ with nanosheet structure was prepared by using mixture of melamine (M) and urea (U) as the precursors for the photocatalytic H₂ production from water. The use of U increased the surface area with mesoporous structure and defects of nitrogen vacancies acting as trap states in g-C₃N₄. The as-obtained g-C₃N₄-M₁U₂ (1 and 2 denote the weight ratios of M and U, respectively) exhibited the photocatalytic H₂ production rate of 3.1 mmol g⁻¹ h⁻¹ under λ ≥ 400 nm light irradiation and apparent quantum efficiency (AQE) of 74% at λ = 400 nm. Single-particle photoluminescence (PL), originated from charge recombination of photogenerated charge carriers, showed longer lifetime of charge carriers in g-C₃N₄-M₁U₂ than that in g-C₃N₄-M. Femtosecond time-resolved diffuse reflectance measurement was performed to observe the photogenerated electrons trapping in g-C₃N₄-M_xU_y. The results show that the electron trapping by the defects as trap states occurs faster in g-C₃N₄-M_xU_y than in g-C₃N₄-M. It is suggested that the use of U increases the defects as electron trap states, leading efficient photocatalytic H₂ production.

1. Introduction

Hydrogen (H₂) is considered as an ideal energy due to its combustion product, H₂O, and high energy density. Since H₂ production from photoelectrochemical water splitting on n-type TiO₂ electrode was discovered by Fujishima and Honda in 1972 [1], great progress has been achieved in photocatalytic H₂ production from renewable resources, mainly water and alcohols. In particular, semiconductors with visible light absorption have attracted much attention because of the ability of photocatalytic H₂ production. Among the various visible-light response photocatalysts, graphitic C₃N₄ (g-C₃N₄), composed of carbon and nitrogen as the earth abundant elements, is therefore one of the suitable candidates as a photocatalyst because of the low cost, good stability, excellent optical, and electronic properties [2–8]. g-C₃N₄ possesses a bandgap around 2.7 eV corresponding to the absorption threshold at 460 nm, and conduction band potential at −1.1 V vs NHE enough for water reduction. So far, many efforts have been done to g-C₃N₄ for improving the photocatalytic activity of H₂ production [9–12].

However, the fast recombination of charge carriers and low surface area lead to the low photocatalytic efficiency and restrict the practical applications of g-C₃N₄. Up to now, numerous effective approaches have been employed to improve the photocatalytic performance of g-C₃N₄

[7,13–16]. Many preparation methods have been used to introduce the defects for trapping photogenerated electrons and decreasing the recombination with holes [17,18]. For example, Chen's group synthesized defect rich g-C₃N₄ by introducing H₂ gas in the thermal condensation process of g-C₃N₄ [18]. In general, g-C₃N₄ is prepared by thermal condensation of thiourea, melamine (M), urea (U), and dicyandiamide. However, the high degree of condensation of precursors gives rise to the samples with a low surface area (~10 m² g⁻¹) and an absence of mesoporous [19]. It is well known that surface area plays an important role in photocatalytic reactions by affording more active sites. The most important technique for the preparation meso-g-C₃N₄ with a large surface area is based on templating methods, such as soft templating (self-assembly) [20] and hard templating (nanocasting) [21]. However, the preparation of meso-g-C₃N₄ with a large surface area is not established.

Herein, we report efficient photocatalytic H₂ production using g-C₃N₄ with increasing defects of nitrogen vacancies and surface area with mesoporous structure. g-C₃N₄-M_xU_y (x and y denote the mass ratios of M to U, respectively) with large surface area and defects were synthesized from a mixture of precursors containing M and U. Previous works showed that several kinds of g-C₃N₄ have been prepared by using mixtures of precursors [22–24]. For example, Ho's group synthesized g-

* Corresponding author.

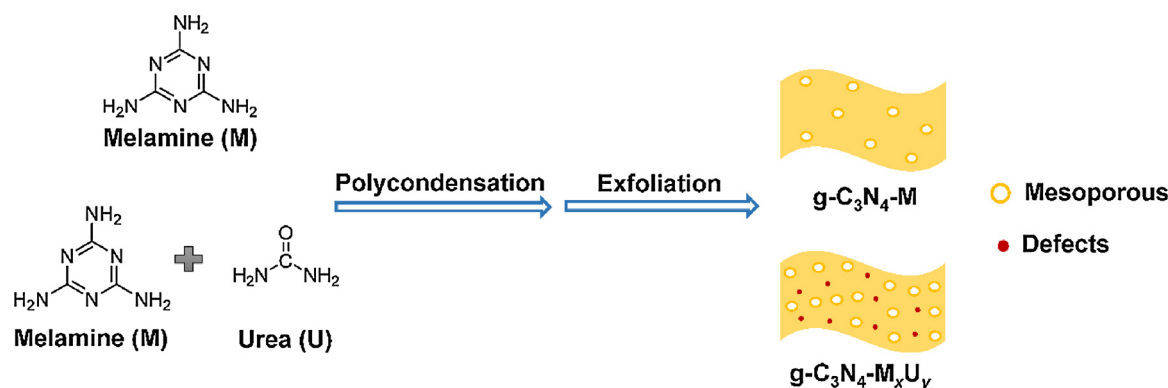
E-mail address: majima@sanken.osaka-u.ac.jp (T. Majima).

<https://doi.org/10.1016/j.apcatb.2018.07.028>

Received 11 June 2018; Received in revised form 2 July 2018; Accepted 8 July 2018

Available online 09 July 2018

0926-3373/ © 2018 Published by Elsevier B.V.



Scheme 1. Preparation of g-C₃N₄-M and g-C₃N₄-M_xU_y using melamine (M) or a mixture of M and urea (U) as the precursors.

C₃N₄/g-C₃N₄ isotype heterojunction by using U and thiourea as the precursors [25]. In the present work, the preparation conditions were optimized by changing the ratios of M and U and the calcination temperatures, and we found that increasing the U content increased the defects and surface area (Scheme 1). U disappeared during the preparation of g-C₃N₄-M_xU_y. The optimum H₂ production rate of g-C₃N₄-M₁U₂ was 3.1 mmol g⁻¹ h⁻¹ under $\lambda \geq 400$ nm light irradiation, and the AQE of 74% at $\lambda = 400$ nm. The enhancement of photocatalytic activity is due to increase in defects and surface area in g-C₃N₄-M₁U₂ which facilitate trapping photogenerated electrons by trap states. The single-particle PL measurement and time-resolved diffuse reflectance spectroscopic measurement were carried out to clarify the dynamics of charges, as well as charge separation and electron injection from photoexcited g-C₃N₄-M_xU_y.

2. Experimental section

2.1. Materials

The bulk g-C₃N₄-M_xU_y, x and y mean the mass ratios of M to U, were prepared by thermal condensation as follows: 2 g of mixture of precursors with x:y from 2:1 to 1:3 were added into 20 ml ethanol. The suspension was stirred at ambient temperature for 0.5 h, then the ethanol was removed by a rotary evaporation apparatus. Subsequently, the mixture powder was put into an alumina crucible with a cover and heated to 773 K for 2 h at a heating rate of 2 K min⁻¹ in a muffle furnace, then rising the temperature to 793 K at the same heating rate for another 2 h. The resulted product was collected and grounded into powder for further use.

g-C₃N₄-M_xU_y with nanosheet structure were prepared as follows: 0.45 g of bulk g-C₃N₄-M_xU_y was uniformly dispersed into a alumina ark with dimensions of 50 × 30 × 10 mm to make sufficient contact between bulk g-C₃N₄-M_xU_y and air, and then heated to 773 K in an open system at a heating rate of 2 K min⁻¹ for 3 h in a muffle furnace. Thus g-C₃N₄-M_xU_y with nanosheet structure were obtained.

For comparison, g-C₃N₄-M and g-C₃N₄-U were also prepared separately by using 2 g of M and 2 g of U under the same calcination conditions. Particularly, the alumina crucible loaded with 2 g of U was empty after the first step calcination. No g-C₃N₄-U was obtained from the same preparation method.

2.2. Characterization of materials

The samples were characterized by X-ray diffraction (XRD, Rigaku, Rint-2500, Cu K α source), SEM (JEOL JSM-6330FT), and TEM (JEOL JEM-2100, operated at 120 kV). UV–vis diffuse reflectance spectra were obtained on a JASCO V-770 UV–vis/NIR spectrophotometer. X-ray photoelectron spectroscopy (XPS) was measured on a JEOL JPS-9010 MC spectrometer. The Brunauer–Emmett–Teller (BET) surface areas

were measured using nitrogen sorption (BEL Japan, BELSORP max). The pore volumes and pore diameter distributions were derived from the adsorption isotherms using the Barrett–Joyner–Halenda (BJH) model.

2.3. Photocatalytic H₂ production measurement

The photocatalytic H₂ production experiments were carried out in a tube with a rubber stopper. Typically, 50 mg samples were dispersed in 50 ml aqueous solution containing 20 vol % TEOA as the sacrificial electron donor. H₂PtCl₆·6H₂O aqueous solution was added as the precursor for the cocatalyst Pt. Then, the suspension was thoroughly degassed under Ar gas flow and irradiated by a xenon lamp (Asahi Spectra, LAX-C100) with magnetic stirring at room temperature. A 400-nm cutoff filter was used to remove the UV light. After 30 min photodeposition of Pt on g-C₃N₄-M_xU_y, the suspension was degassed again. H₂ production was measured by using Shimadzu GC-8 A gas chromatograph equipped with an MS-5 A column and a thermal conductivity detector. The apparent quantum efficiency (AQE) for H₂ production at different wavelengths of the monochromatic light was calculated via the following equation: AQE = (2 × number of H₂ molecules/number of incident photons) × 100%. The light intensity at $\lambda = 400$ nm, 420 nm, 440 nm and 460 nm were 680 μ W cm⁻², 1.72 mW cm⁻², 1.44 mW cm⁻² and 1.77 mW cm⁻², respectively. The light intensity was measured by an optical power meter (1916-R, Newport). The irradiation area was 0.785 cm².

2.4. Photoelectrochemical measurement

Photoelectrochemical measurements were carried out in a standard three-electrode quartz cell with a platinum wire as the counter electrode, Ag/AgCl electrodes as the reference electrode, g-C₃N₄-M_xU_y modified glass carbon electrode as the working electrode, and 0.5 M Na₂SO₄ aqueous solution as the electrolyte. The photocurrent responses and EIS spectra were recorded at an electrode potential of 0.3 V with a scan rate of 25 mV s⁻¹. The working electrode was irradiated by a xenon lamp (Asahi Spectra, HAL-320 W) with a 400 nm cutoff filters. All measurements were carried out at room temperature.

2.5. Single-particle PL measurement by confocal microscopy

Sample preparation for single-particle PL experiments was carried out as follows. The cover glasses were purchased from DAICO MFG CO., Ltd. (Japan) and cleaned by sonication in a 20% detergent solution (As One, Cleanace) for 7 h, followed by repeated washing with warm water 5 times. g-C₃N₄-M_xU_y were well dispersed in ethanol solution and then were spin-coated on the cleaned cover glasses. The cover glasses were annealed at 100 °C for 1 h to immobilize the particles on the surface.

Single-particle PL images and spectra of samples were recorded by

using an objective scanning confocal microscope system (PicoQuant, MicroTime 200) coupled with an Olympus IX71 inverted fluorescence microscope. The samples were excited through an oil-immersion objective lens (Olympus, UplanSApochromat, $100\times$, 1.4 NA) with a circular-polarized 405 nm picoseconds pulsed laser controlled by a PDL-800B driver (PicoQuant). Typical excitation powers for the PL measurements were 120 μW at the sample. The emission from the sample was collected by the same objective and detected by a single photon avalanche photodiode (Micro Photon Devices, PDM 50 CT) through a dichroic beam splitter (Chroma, 405rdc) and long pass filter (Chroma, HQ430CP). For the spectroscopy, only the emission that passed through a slit entered the imaging spectrograph (Acton Research, SP-2356) that was equipped with an electron-multiplying charge-coupled device (EMCCD) camera (Princeton Instruments, ProEM). All experimental data were obtained at room temperature.

2.6. Time-resolved diffuse reflectance transient absorption measurement

The femtosecond diffuse reflectance transient absorption spectra were measured by the pump and probe method using a regeneratively amplified titanium sapphire laser (SpectraPhysics, Spitfire Pro F, 1 kHz) pumped by a Nd:YLF laser (Spectra-Physics, Empower 15). The second harmonic oscillation of the amplifier (400 nm, 3 μJ per pulse) was used as the excitation pulse. A white light continuum pulse, generated by focusing the residual of the fundamental light on a sapphire crystal, was directed to the sample powder coated on the glass substrate, and the reflected lights were detected by using a linear InGaAs array detector equipped with a polychromator (Solar, MS3504). All measurements were carried out at room temperature.

3. Results and discussion

3.1. Material preparation and characterization

The X-ray diffraction (XRD) patterns of all samples reveal the formation of graphite like stacking C_3N_4 layers as shown in Fig. 1a. The peaks observed around 13.0° correspond to the in-plane tri-s-triazine units. The strongest peaks around 27.5° is indexed to the (002) plane, demonstrating the graphite-like stacking of the conjugated aromatic units [22]. Compared with $\text{g-C}_3\text{N}_4\text{-M}$, $\text{g-C}_3\text{N}_4\text{-M}_x\text{U}_y$ showed no XRD peak shift, indicating that U as one of precursors disappeared during the preparation of $\text{g-C}_3\text{N}_4\text{-M}_x\text{U}_y$. It is reported that van der Waals force between layers exists in $\text{g-C}_3\text{N}_4$. The intensity of the (002) diffraction peaks of $\text{g-C}_3\text{N}_4\text{-M}_x\text{U}_y$ was found to decrease gradually with increasing the mass ratio of U, suggesting the effective exfoliation of bulk $\text{g-C}_3\text{N}_4$ into nanosheets through overcoming the weak van der Waals force between layers during the further thermal treatment [26]. In order to confirm the molecular structure of the prepared $\text{g-C}_3\text{N}_4\text{-M}_x\text{U}_y$, FT-IR measurements were applied. All samples showed a peak at 810 cm^{-1} in

FT-IR spectra to be assigned to the out-of-plane bending mode of heptazine rings, while peaks in the range of 900 and 1800 cm^{-1} correspond to N-C=N heterorings in the “melon” framework. The broad band in the range of $3000\text{--}3500\text{ cm}^{-1}$ is assigned to uncondensed amine groups generated from the synthesis of the photocatalysts as well as water molecules adsorbed on the surface [27]. Using the mixture of precursors promotes the planarization of $\text{g-C}_3\text{N}_4$ layers as shown in Fig. S1, decreasing the interaction between two neighboring atoms separately located in two adjacent tri-s-triazine rings. Therefore, these atoms vibrate more vigorously because of less restraint, resulting in better distinguished vibration bands as shown in Fig. 1b [23]. There is neither new peak nor shifted peak, suggesting that U does not influence on the molecular structure of $\text{g-C}_3\text{N}_4\text{-M}_x\text{U}_y$.

The morphology and microstructure of all samples were characterized by scanning electron microscopy (SEM) and transmission electron microscopy (TEM). $\text{g-C}_3\text{N}_4\text{-M}$ possesses a thick 2D sheet-like structure, while $\text{g-C}_3\text{N}_4\text{-M}_x\text{U}_y$ with nanosheet structure are smoother and thinner as shown in SEM images (Fig. S1). All $\text{g-C}_3\text{N}_4\text{-M}_x\text{U}_y$ possess a large number of in-plane mesoporous distributed in the entire $\text{g-C}_3\text{N}_4\text{-M}_x\text{U}_y$ layers to offer new exposed active sites as shown in Fig. 2. The surface areas and pore structures of all samples were measured by N_2 adsorption-desorption measurements. As shown in Fig. S2, all curves exhibit a typical IV isotherm, assigned to the presence of mesoporous (2–50 nm). The hysteresis loops are classified as a type of H3, indicating the slit-shaped pores in nanosheet materials. The surface areas and pore parameters are summarized in Table 1. In comparison with $\text{g-C}_3\text{N}_4\text{-M}$, the BET surface areas of $\text{g-C}_3\text{N}_4\text{-M}_x\text{U}_y$ improve gradually with increasing the mass ratio of U mainly due to the presence of oxygen in U precursor, inducing the formation of CO_2 during the polymerization [28]. It is well known that higher surface area is preferable for photocatalytic efficiency by affording more active sites. $\text{g-C}_3\text{N}_4\text{-M}_1\text{U}_2$ shows the highest efficiency of the photocatalytic H_2 production. The BET surface area of $\text{g-C}_3\text{N}_4\text{-M}_1\text{U}_2$ is $233\text{ m}^2\text{ g}^{-1}$, that is 2 times higher than that of $\text{g-C}_3\text{N}_4\text{-M}$. Except $\text{g-C}_3\text{N}_4\text{-M}_1\text{U}_3$, the pore size distribution curves of $\text{g-C}_3\text{N}_4\text{-M}_x\text{U}_y$ have a sharpness peak at 2.4–3.0 nm. Although $\text{g-C}_3\text{N}_4\text{-M}_1\text{U}_3$ reveals the largest surface area of $299\text{ m}^2\text{ g}^{-1}$, the pore diameter (37.9 nm) indicates that excessive U leads to the collapse of the nanosheet structure. The disappeared mesoporous results in the low efficiency of the photocatalytic H_2 production because of less active sites.

The UV–vis diffuse-reflectance spectra (DRS) of $\text{g-C}_3\text{N}_4\text{-M}_x\text{U}_y$ are presented in Fig. 3a. The band gap energies (E_g) estimated from the plots of $(\alpha h\nu)^{1/2}$ vs photon energy are 2.64, 2.60, 2.60, 2.60, and 2.61 eV for $\text{g-C}_3\text{N}_4\text{-M}$, $\text{g-C}_3\text{N}_4\text{-M}_2\text{U}_1$, $\text{g-C}_3\text{N}_4\text{-M}_1\text{U}_1$, $\text{g-C}_3\text{N}_4\text{-M}_1\text{U}_2$, and $\text{g-C}_3\text{N}_4\text{-M}_1\text{U}_3$, respectively, as shown in Fig. 3b–f. $\text{g-C}_3\text{N}_4\text{-M}_x\text{U}_y$ have more intense absorption in the visible light region compared with $\text{g-C}_3\text{N}_4\text{-M}$, primarily resulting from multiple scattering effect associated with their porous structure [29]. Elemental analysis was employed to investigate the defect type in $\text{g-C}_3\text{N}_4\text{-M}_x\text{U}_y$ as shown in Table S1. The results show that the C/N atomic ratio gradually increased from 0.650 in $\text{g-C}_3\text{N}_4\text{-M}$

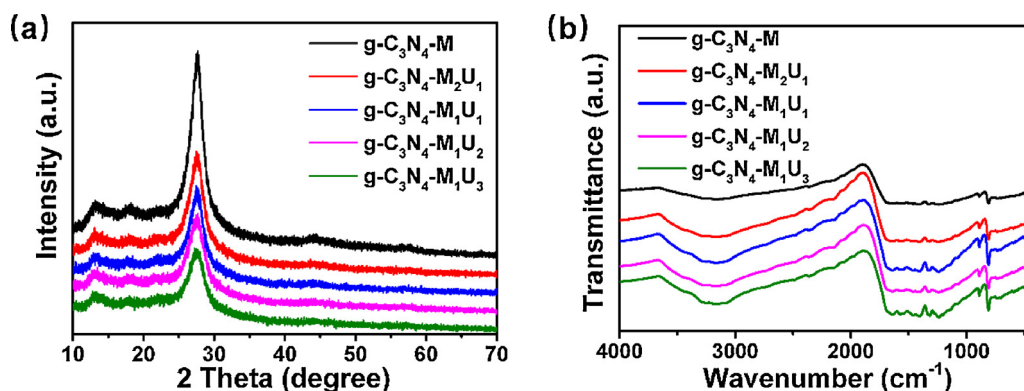


Fig. 1. XRD patterns (a) and FT-IR spectra (b) of $\text{g-C}_3\text{N}_4\text{-M}$ and $\text{g-C}_3\text{N}_4\text{-M}_x\text{U}_y$.

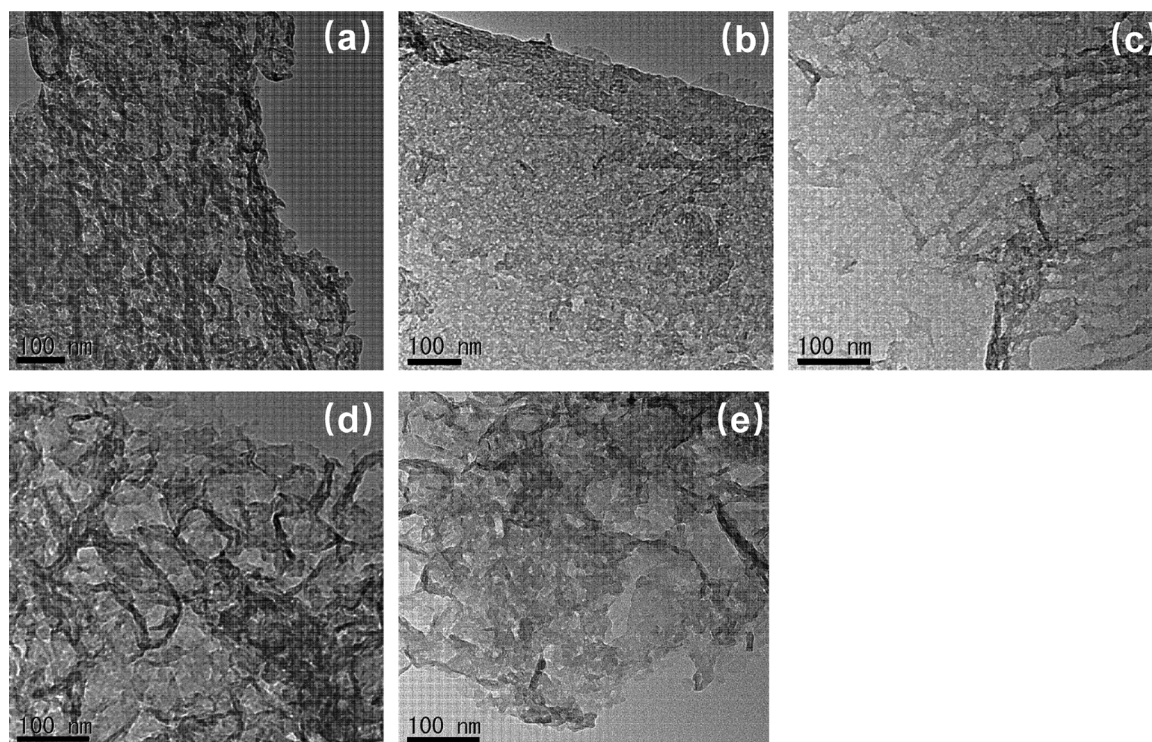


Fig. 2. TEM images of g-C₃N₄-M (a), g-C₃N₄-M₂U₁ (b), g-C₃N₄-M₁U₁ (c), g-C₃N₄-M₁U₂ (d), and g-C₃N₄-M₁U₃ (e).

Table 1

Surface areas and pore parameters of g-C₃N₄-M and g-C₃N₄-M_xU_y.

Sample	Surface area (m ² g ⁻¹)	Pore volume (cm ³ g ⁻¹)	Pore diameter ^a (nm)
g-C ₃ N ₄ -M	116	0.424	2.8/14.6
g-C ₃ N ₄ -M ₂ U ₁	189	1.12	2.7/23.7
g-C ₃ N ₄ -M ₁ U ₁	211	1.46	2.4/27.8
g-C ₃ N ₄ -M ₁ U ₂	233	1.57	3.0/27.0
g-C ₃ N ₄ -M ₁ U ₃	299	3.15	37.9/42.1

^a The small and large mesopore diameters are ascribed to the pores within the layer and stacking layers, respectively [24].

to 0.659 in g-C₃N₄-M₁U₃. Thus, the urea (U) induced defects derived from the formation of the nitrogen vacancies in g-C₃N₄-M_xU_y [30]. This can explain the slightly narrowed bandgap and enhanced visible light absorption by nitrogen vacancies [31]. It is reported that nitrogen vacancies in the g-C₃N₄ potentially results in additional electron states below the conduction band [18].

The XPS measurements were carried out to clarify the chemical state of the surface elements of samples as shown in Fig. 4 and S3. The C 1 s spectra of g-C₃N₄-M and g-C₃N₄-M₁U₂ exhibit two peaks at the binding energy of 288.5 and 286.1 eV identified to N–C = N coordination in the framework and C–NH₂ on the edges of heptazine units, respectively [32,33]. The N 1 s signals in Fig. 4b and d are deconvoluted into three peaks with the binding energies at 398.8, 399.5, and 401.2 eV, assigned to sp² N atoms in triazine ring (C–N = C), bridging N atoms (N(C₃)), and N–H groups, respectively [24,34].

3.2. Photocatalytic activity

The photocatalytic activities of all samples were evaluated by H₂ production rate under visible light irradiation ($\lambda \geq 400$ nm). As shown in Fig. 5a, all samples with loading 3.0 wt% Pt as cocatalyst showed the photocatalytic H₂ production. The time-dependent photocatalytic H₂ production over different photocatalysts under visible light irradiation ($\lambda \geq 400$ nm) are shown in Fig. S4. The H₂ production rate increased

gradually with increasing the mass ratio of M to U from 2:1 to 1:2. The H₂ production rate of g-C₃N₄-M₁U₂ was calculated to be 3.1 mmol g⁻¹ h⁻¹ and 3.7 times higher than that of g-C₃N₄-M (0.8 mmol g⁻¹ h⁻¹). The enhanced activity can be attributed to the facts that g-C₃N₄-M₁U₂ has larger surface area and more mesoporous to enhance the electron transfer and offer more active sites compared with g-C₃N₄-M. Besides, the disappeared U results in the formation of defects as the trap states for the photogenerated electrons, leading to high separation efficiency of the photogenerated charge carriers. Obviously, U plays an important role in the formation of defects in g-C₃N₄-M_xU_y. Although g-C₃N₄-M₁U₃ possesses the largest surface area reached to 299 m² g⁻¹, the photocatalytic activity is not so high to suggest that other factors rather than the surface area are responsible for the photocatalytic efficiency. The photocatalytic activity of g-C₃N₄-M₁U₃ decreases with increasing the mass ratio of M to U to 1:3, suggesting that the excessive U induced collapse of the nanosheet structure and less active sites due to the disappeared mesoporous as shown in the TEM image (Fig. 2e). Cycling experiments were carried out to evaluate the stability of g-C₃N₄-M₁U₂ photocatalyst. The H₂ production rate of g-C₃N₄-M₁U₂ after four cycling was sustained and no significant variation was confirmed as shown in Fig. 5b, indicating the stability of g-C₃N₄-M₁U₂ photocatalyst. The apparent quantum efficiency (AQE) of g-C₃N₄-M₁U₂ was estimated to be 74% at $\lambda = 400$ nm and 28% at $\lambda = 420$ nm (Fig. 6).

The photocurrents of all samples were measured via several on-off cycles of intermittent visible light irradiation, directly correlating with the separation efficiency of the photogenerated charge carriers. As shown in Fig. 7a, the photocurrent responses of all samples were stable and reproducible in the time scale of 30–240 s. The photocurrent of g-C₃N₄-M₁U₂ was significantly higher than that of other samples due to larger surface area with mesoporous and larger defects, facilitating the electron transfer and the separation of the photogenerated charge carriers. Furthermore, electrochemical impedance spectroscopy (EIS) was measured to clarify the electrical conductivity of all samples. As shown in Fig. 7b, a smaller arc radius of the EIS Nyquist plot indicates an effective separation of photogenerated electron–hole pairs and fast interfacial charge transfer. The enhanced photoelectric properties of g-

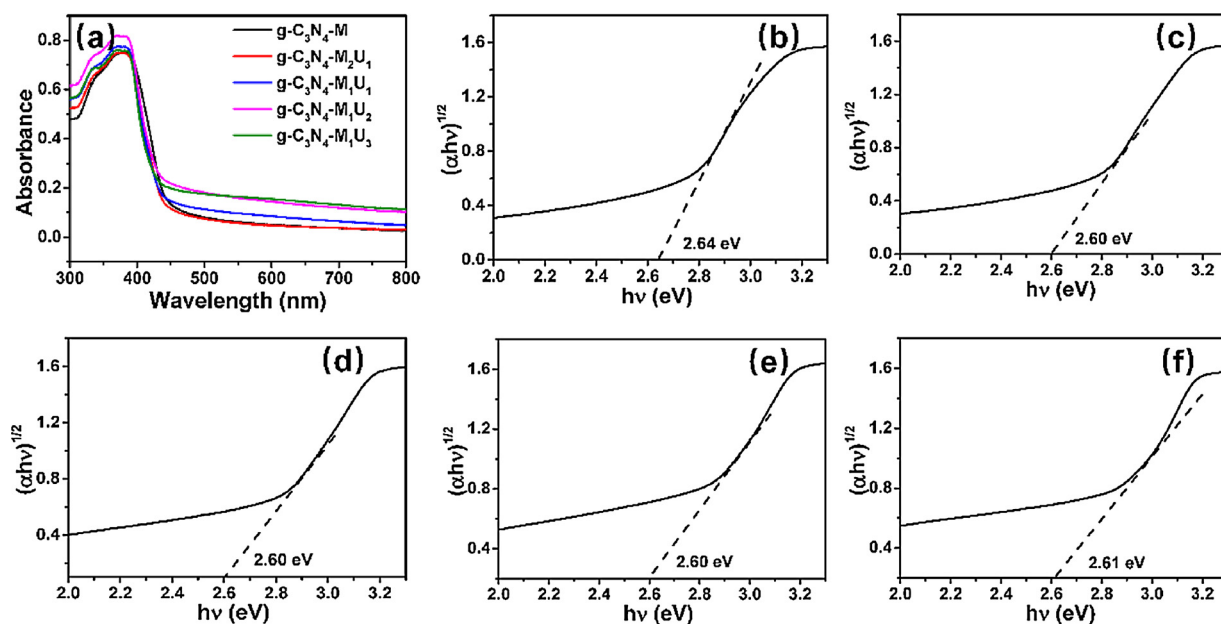


Fig. 3. UV-vis DRS (a) of all samples and plots of $(\alpha h\nu)^{1/2}$ vs photo energy of $g\text{-C}_3\text{N}_4\text{-M}$ (b), $g\text{-C}_3\text{N}_4\text{-M}_2\text{U}_1$ (c), $g\text{-C}_3\text{N}_4\text{-M}_1\text{U}_1$ (d), $g\text{-C}_3\text{N}_4\text{-M}_1\text{U}_2$ (e), and $g\text{-C}_3\text{N}_4\text{-M}_1\text{U}_3$ (f).

$\text{C}_3\text{N}_4\text{-M}_1\text{U}_2$ are attributable to the larger surface area to improve greatly photogenerated charge mobility.

3.3. Single-particle PL measurement

Single-particle photoluminescence (PL) was used to elucidate the separation and transfer mechanism of charge carriers [35,36] as well as the role of U in the formation of $g\text{-C}_3\text{N}_4\text{-M}_x\text{U}_y$. The excitation source is a circularly polarized 405-nm laser. PL images of all samples are shown in Fig. 8a–e. Five locations were randomly chosen for each sample to be marked with Arabic numbers in the images. The representative PL

spectra of $g\text{-C}_3\text{N}_4\text{-M}_x\text{U}_y$ at the position numbered “1” are shown in Fig. 8f, while the PL intensities of other four locations as numbered from “2” to “5” are shown in Fig. S4. The PL intensity gradually decreased with increasing the mass ratio of M to U from 2:1 to 1:2, indicating a slower recombination rate of the photogenerated charge carriers in $g\text{-C}_3\text{N}_4\text{-M}_1\text{U}_2$. Similar results were obtained from different positions of the same cover glass for all samples as shown in Figs. S5–S7. The average PL lifetimes of $g\text{-C}_3\text{N}_4\text{-M}_x\text{U}_y$ represent the recombination of charge carriers with short and long distances which are shown by red arrows in Fig. 10b. Fig. 8 show that the emission process of $g\text{-C}_3\text{N}_4\text{-M}_x\text{U}_y$ suppresses significantly and the resulting PL lifetime

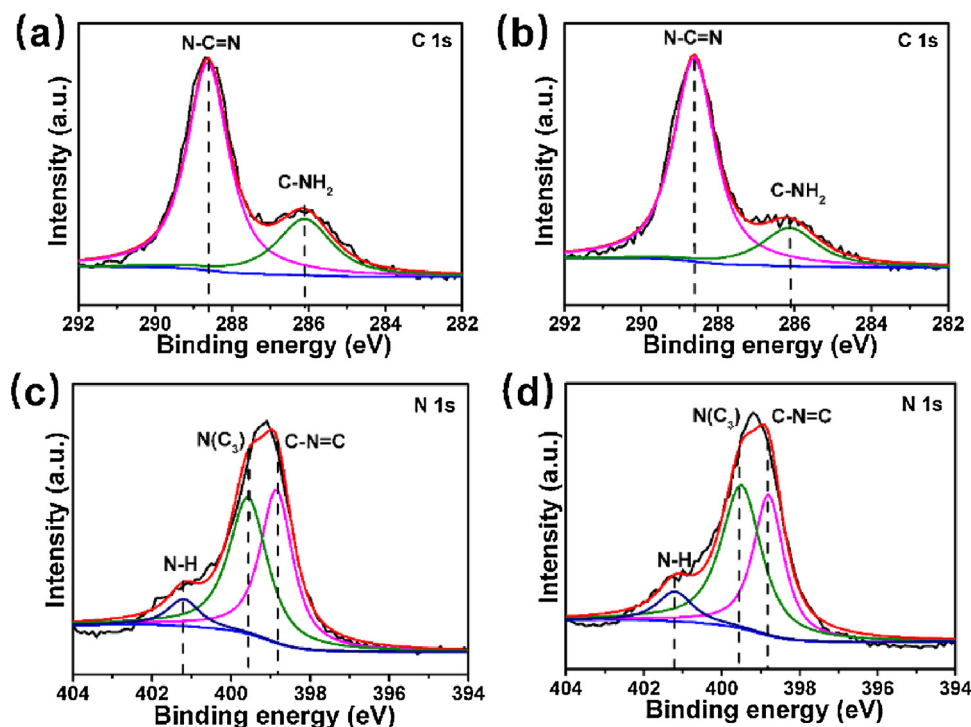


Fig. 4. XPS spectra of C 1s and N 1s of $g\text{-C}_3\text{N}_4\text{-M}$ (a and c) and $g\text{-C}_3\text{N}_4\text{-M}_1\text{U}_2$ (b and d).

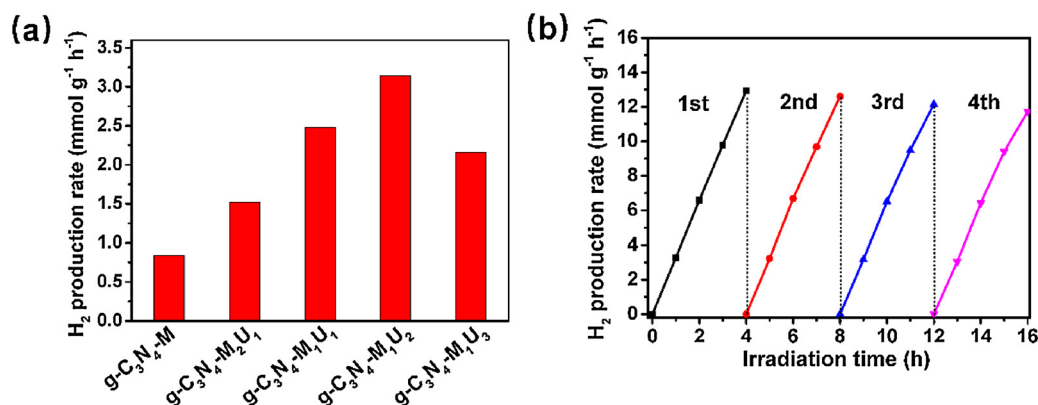


Fig. 5. Photocatalytic H₂ production rate for g-C₃N₄-M and g-C₃N₄-M_xU_y (a) and cycling test of photocatalytic H₂ production for g-C₃N₄-M₁U₂ (b).

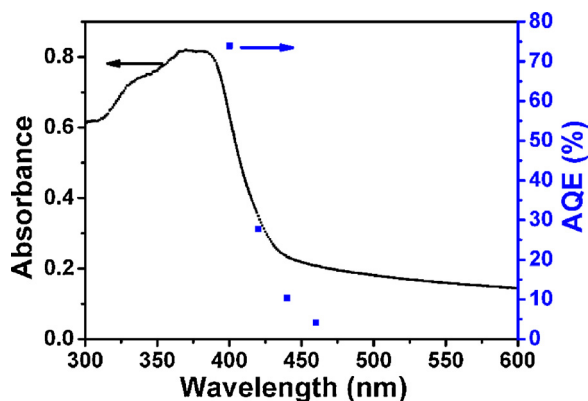


Fig. 6. Absorption spectrum and wavelength-dependent apparent quantum efficiency (AQE) of photocatalytic H₂ production for g-C₃N₄-M₁U₂.

was 3.5 ns for g-C₃N₄-M₁U₂ and 1.42 times longer than that of g-C₃N₄-M as shown in Fig. 9, indicating that g-C₃N₄-M_xU_y possesses the slower recombination process with the longer lifetime of photogenerated electrons than g-C₃N₄-M. Similar to the discussion on the photocatalytic activity for foam-like holey ultrathin g-C₃N₄ [37], more electrons transfer to Pt nanoparticles in g-C₃N₄-M₁U₂ to give a higher yield of H₂ production than in g-C₃N₄-M. For g-C₃N₄-M₁U₃, the decreased lifetime is probably due to the excessive defects derived from disappeared U could serve as recombination centers for the electrons and holes. The photoluminescence lifetime of g-C₃N₄-M₁U₃ is short than that of g-C₃N₄-M₁U₂, which indicates that recombination of charge carriers occur faster in g-C₃N₄-M₁U₃ than that in g-C₃N₄-M₁U₂. Thus, it is considered that excessive defects could act as recombination centers. It is reported that overintroduction of nitrogen vacancies could generate the deeper midgap states that act as recombination sites [45].

3.4. Time-resolved diffuse reflectance measurement

Time-resolved diffuse reflectance (TDR) measurement provides the charge lifetimes and charge transfer processes [38–40] of g-C₃N₄-M_xU_y under visible light irradiation. The TDR spectra of all samples were recorded at various times after the 400-nm laser flash excitation. Upon the visible light irradiation to g-C₃N₄-M_xU_y, electrons and holes are generated in CB and VB, respectively. A broad transient absorption signal in the range of 850–1150 nm [7], assigned to the trapped and free electrons in the semiconductors, was observed for all samples as shown in Fig. S8. For all samples, the transient absorption signals reached the highest intensities immediately after a 400-nm laser flash irradiation, and then gradually decayed. To elucidate the decay kinetics, the time profiles of the transient absorption at 950 nm for all samples were fitted by two-exponential functions as shown in Fig. 10a, and their lifetimes are summarized in Table 2. It is known that successive pathways of exciton relaxation to electron trap states with different trap distances are analyzed by two decay time constants [41].

The decay profiles of g-C₃N₄-M_xU_y were fitted by a two-exponential decay function with short and long lifetimes τ_1 and τ_2 , corresponding to the trapping of electrons by the defects at short and long distances, respectively. The decay average lifetimes of g-C₃N₄-M_xU_y decrease compared with that of g-C₃N₄-M ($\tau_{av} = 911$ ps), indicating the existence of an additional channel for electron transfer from the semiconductor CB to the electron trap states. Recently, Durrant et al. reported that the initial charge trapping in carbon nitride sample occurs at < 1 ns [42]. The decay profile of transient absorption for g-C₃N₄-M was fitted with a short lifetime τ_1 (52 ps, 27%) and long lifetime τ_2 (1229 ps, 73%), suggesting that photogenerated electrons could be trapped by the defects at short and long distances at τ_1 and τ_2 , respectively. For g-C₃N₄-M_xU_y sample, τ_1 and τ_2 decrease gradually with increasing the density of defects by increasing the mass ratio of U as shown in Fig. S8. The photogenerated electrons in g-C₃N₄-M_xU_y are trapped by the defects at

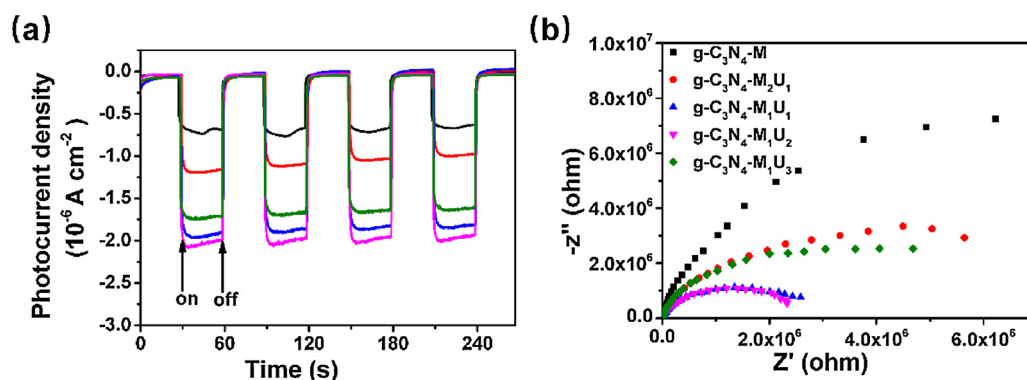


Fig. 7. Photocurrent response (a) and EIS (b) for g-C₃N₄-M and g-C₃N₄-M_xU_y.

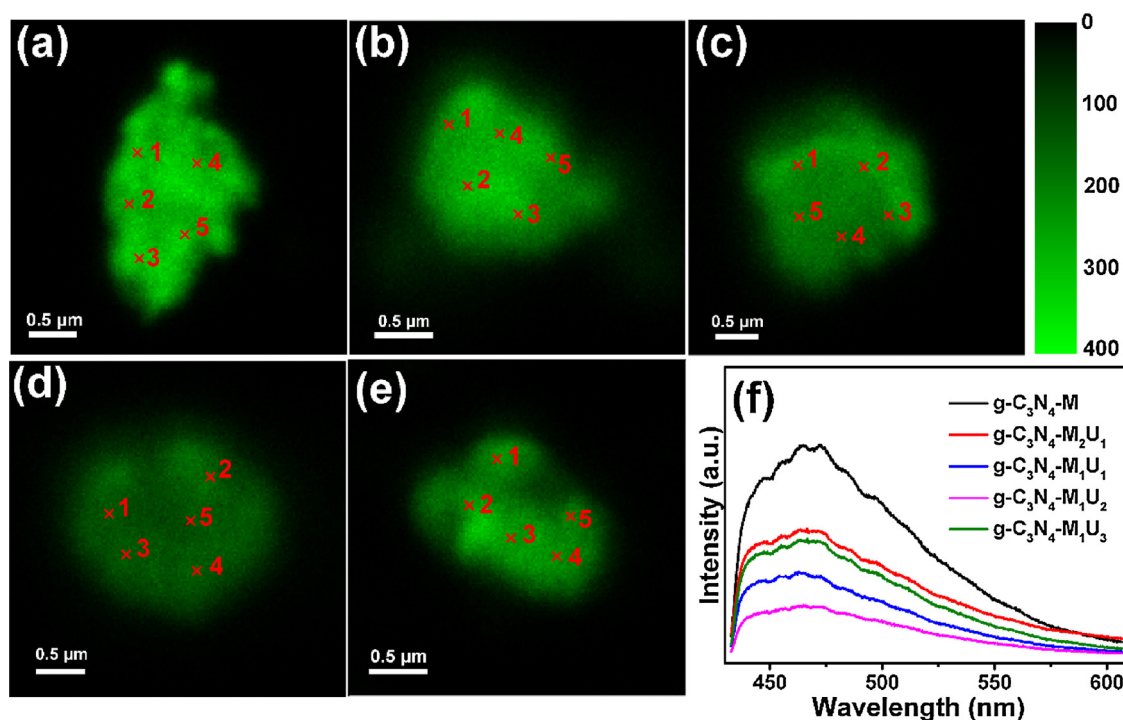


Fig. 8. PL images of $g\text{-C}_3\text{N}_4\text{-M}_x\text{U}_y$ on a quartz cover glass. $g\text{-C}_3\text{N}_4\text{-M}$ (a), $g\text{-C}_3\text{N}_4\text{-M}_2\text{U}_1$ (b), $g\text{-C}_3\text{N}_4\text{-M}_1\text{U}_1$ (c), $g\text{-C}_3\text{N}_4\text{-M}_1\text{U}_2$ (d), and $g\text{-C}_3\text{N}_4\text{-M}_1\text{U}_3$ (e). Representative PL spectra of $g\text{-C}_3\text{N}_4\text{-M}_x\text{U}_y$ as numbered “1” in (a)–(e).

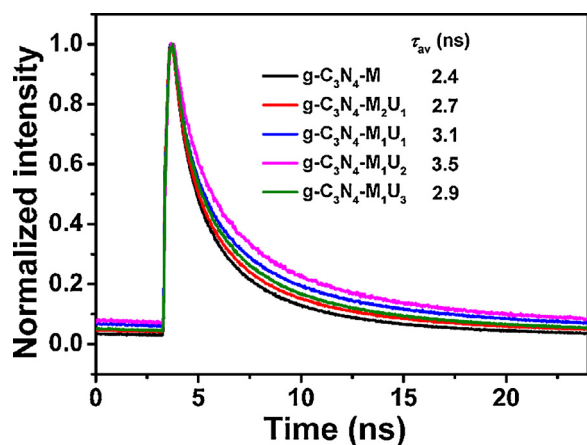


Fig. 9. PL decay profiles of $g\text{-C}_3\text{N}_4\text{-M}$ and $g\text{-C}_3\text{N}_4\text{-M}_x\text{U}_y$.

Table 2

Lifetimes of TDR decays for all samples under 400-nm irradiation.

Sample	τ_1 (ps)	τ_2 (ps)	τ_{av} (ps)
$g\text{-C}_3\text{N}_4\text{-M}$	52 ± 9 (27 %)	1229 ± 258 (73 %)	911
$g\text{-C}_3\text{N}_4\text{-M}_2\text{U}_1$	29 ± 10 (25 %)	476 ± 94 (75 %)	364
$g\text{-C}_3\text{N}_4\text{-M}_1\text{U}_1$	41 ± 13 (24 %)	712 ± 81 (76 %)	551
$g\text{-C}_3\text{N}_4\text{-M}_1\text{U}_2$	24 ± 10 (28 %)	628 ± 87 (72 %)	459
$g\text{-C}_3\text{N}_4\text{-M}_1\text{U}_3$	24 ± 7 (30 %)	409 ± 56 (70 %)	294

short distances in the time scale of 24–41 ps to be shorter than $\tau_1 = 52$ ps for $g\text{-C}_3\text{N}_4\text{-M}$. Recently, several studies have indicated that charge trapping derived from defects plays a crucial role in photocatalytic activity of carbon nitride materials [31,43,44]. In our experiments, an increase of U leads an increase of defects acting as the electron trap states of photogenerated electrons, resulting in a shorter τ_2 . Therefore, the long distance trapping of the photogenerated electrons could be retarded. The photogenerated electrons of defect rich $g\text{-C}_3\text{N}_4\text{-M}_x\text{U}_y$ are trapped by the defects with short and long distances at

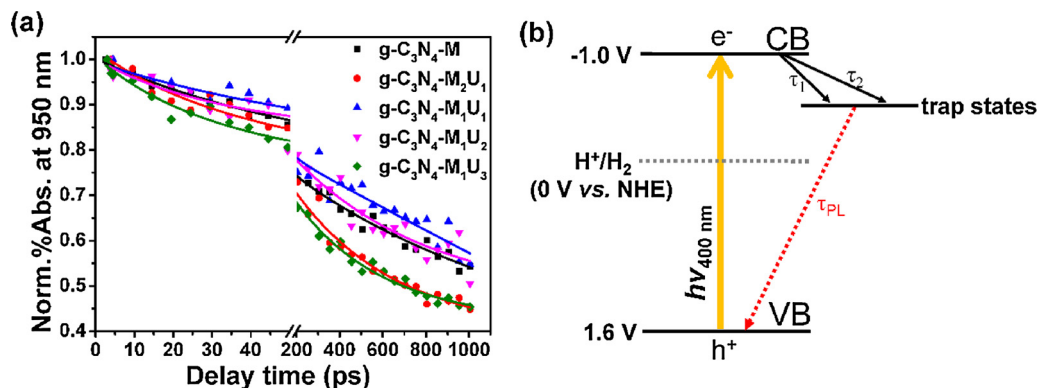


Fig. 10. Time profiles of normalized transient absorption at 950 nm for all samples after 400-nm laser irradiation (a) and schematic illustration of photogenerated electron trapping by the trap states in $g\text{-C}_3\text{N}_4\text{-M}_x\text{U}_y$ (b).

τ_1 and τ_2 which are shorter than $\tau_1 = 52$ and $\tau_2 = 1229$ ps for g-C₃N₄-M, respectively, as illustrated in Fig. 10b. It has been reported that electron transfer from carbon nitride to cocatalyst Pt in the ns timescale which competes with electron trapping in carbon nitride [42]. Therefore, more electrons transfer from g-C₃N₄-M_xU_y to Pt nanoparticles compared with g-C₃N₄-M, resulting in efficient production of H₂.

4. Conclusion

Defects rich g-C₃N₄-M_xU_y with high surface area, mesoporous, nanosheet structure were synthesized by using a mixture of M and U as the precursors. Femtosecond time-resolved diffuse reflectance measurements reveal that photogenerated electrons in CB of g-C₃N₄-M_xU_y are trapped by the defects of nitrogen vacancies. g-C₃N₄-M₁U₂ exhibits a large H₂ production rate of 3.1 mmol g⁻¹ h⁻¹ under visible light irradiation and AQE estimated of 74% at $\lambda = 400$ nm. U plays a crucial role in enhancement of photocatalytic performance by improving surface area and efficient photogenerated electron trapping. The present work provides a simple method for synthesis of defect rich carbon nitride with high surface area to exhibit the efficient photocatalytic activity.

Acknowledgements

This work was partly supported by a Grant-in-Aid for Scientific Research (Project 25220806 and others) from the Ministry of Education, Culture, Sports, Science and Technology (MEXT) of the Japanese Government. We are thankful for the help of the Comprehensive Analysis Center of SANKEN, Osaka University. DR thanks the China Scholarship Council for scholarship (No. 201608310114).

Appendix A. Supplementary data

Supplementary material related to this article can be found, in the online version, at doi:<https://doi.org/10.1016/j.apcatb.2018.07.028>.

References

- [1] A. Fujishima, K. Honda, Electrochemical photolysis of water at a semiconductor electrode, *Nature* 238 (1972) 37.
- [2] X. Wang, K. Maeda, A. Thomas, K. Takanebe, G. Xin, J.M. Carlsson, K. Domen, M. Antonietti, A metal-free polymeric photocatalyst for hydrogen production from water under visible light, *Nat. Mater.* 8 (2009) 76–80.
- [3] G.-h. Moon, M. Fujitsuka, S. Kim, T. Majima, X. Wang, W. Choi, Eco-friendly photochemical production of H₂O₂ through O₂ reduction over carbon nitride frameworks incorporated with multiple heteroelements, *ACS Catal.* 7 (2017) 2886–2895.
- [4] C. Pan, J. Xu, Y. Wang, D. Li, Y. Zhu, Dramatic activity of C₃N₄/BiPO₄ photocatalyst with core/shell structure formed by self-assembly, *Adv. Funct. Mater.* 22 (2012) 1518–1524.
- [5] X. Bai, L. Wang, R. Zong, Y. Zhu, Photocatalytic activity enhanced via g-C₃N₄ nanoplates to nanorods, *J. Phys. Chem. C* 117 (2013) 9952–9961.
- [6] L. Lin, W. Ren, C. Wang, A.M. Asiri, J. Zhang, X. Wang, Crystalline carbon nitride semiconductors prepared at different temperatures for photocatalytic hydrogen production, *Appl. Catal. B: Environ.* 231 (2018) 234–241.
- [7] M. Zhu, S. Kim, L. Mao, M. Fujitsuka, J. Zhang, X. Wang, T. Majima, Metal-free photocatalyst for H₂ evolution in visible to near-infrared region: black phosphorus/graphitic carbon nitride, *J. Am. Chem. Soc.* 139 (2017) 13234–13242.
- [8] M.Q. Wen, T. Xiong, Z.G. Zang, W. Wei, X.S. Tang, F. Dong, Synthesis of MoS₂/g-C₃N₄ nanocomposites with enhanced visible-light photocatalytic activity for the removal of nitric oxide (NO), *Opt. Express* 24 (2016) 10205–10212.
- [9] P. Niu, L. Zhang, G. Liu, H.-M. Cheng, Graphene-like carbon nitride nanosheets for improved photocatalytic activities, *Adv. Funct. Mater.* 22 (2012) 4763–4770.
- [10] H. Ou, L. Lin, Y. Zheng, P. Yang, Y. Fang, X. Wang, Tri-s-triazine-based crystalline carbon nitride nanosheets for an improved hydrogen evolution, *Adv. Mater.* 29 (2017) 1700008.
- [11] P. Yang, H. Ou, Y. Fang, X. Wang, A facile steam reforming strategy to delaminate layered carbon nitride semiconductors for photoredox catalysis, *Angew. Chem. Int. Ed. Engl.* 56 (2017) 3992–3996.
- [12] Z. Lin, X. Wang, Nanostructure engineering and doping of conjugated carbon nitride semiconductors for hydrogen photosynthesis, *Angew. Chem. Int. Ed.* 52 (2013) 1735–1738.
- [13] G. Liu, T. Wang, H. Zhang, X. Meng, D. Hao, K. Chang, P. Li, T. Kako, J. Ye, Nature-inspired environmental "phosphorylation" boosts photocatalytic H₂ production over carbon nitride nanosheets under visible-light irradiation, *Angew. Chem. Int. Ed. Engl.* 54 (2015) 13561–13565.
- [14] W. Liu, L. Cao, W. Cheng, Y. Cao, X. Liu, W. Zhang, X. Mou, L. Jin, X. Zheng, W. Che, Q. Liu, T. Yao, S. Wei, Single-site active cobalt-based photocatalyst with a long carrier lifetime for spontaneous overall water splitting, *Angew. Chem. Int. Ed. Engl.* 56 (2017) 9312–9317.
- [15] X. Shi, M. Fujitsuka, Z. Lou, P. Zhang, T. Majima, In situ nitrogen-doped hollow-TiO₂/g-C₃N₄ composite photocatalysts with efficient charge separation boosting water reduction under visible light, *J. Mater. Chem. A* 5 (2017) 9671–9681.
- [16] D. Zheng, X.N. Cao, X. Wang, Precise formation of a hollow carbon nitride structure with a janus surface to promote water splitting by photoredox catalysis, *Angew. Chem. Int. Ed. Engl.* 55 (2016) 11512–11516.
- [17] B.-W. Sun, H.-J. Li, H.-y. Yu, D.-J. Qian, M. Chen, In situ synthesis of polymetallic Co-doped g-C₃N₄ photocatalyst with increased defect sites and superior charge carrier properties, *Carbon* 117 (2017) 1–11.
- [18] Q. Tay, P. Kanhere, C.F. Ng, S. Chen, S. Chakraborty, A.C.H. Huan, T.C. Sum, R. Ahuja, Z. Chen, Defect engineered g-C₃N₄ for efficient visible light photocatalytic hydrogen production, *Chem. Mater.* 27 (2015) 4930–4933.
- [19] S. Patnaik, S. Martha, K.M. Parida, An overview of the structural, textural and morphological modulations of g-C₃N₄ towards photocatalytic hydrogen production, *RSC Adv.* 6 (2016) 46929–46951.
- [20] Y. Wang, X. Wang, M. Antonietti, Polymeric graphitic carbon nitride as a heterogeneous organocatalyst: from photochemistry to multipurpose catalysis to sustainable chemistry, *Angew. Chem. Int. Ed. Engl.* 51 (2012) 68–89.
- [21] M. Groenewolt, M. Antonietti, Synthesis of g-C₃N₄ nanoparticles in mesoporous silica host matrices, *Adv. Mater.* 17 (2005) 1789–1792.
- [22] S. Martha, A. Nashim, K.M. Parida, Facile synthesis of highly active g-C₃N₄ for efficient hydrogen production under visible light, *J. Mater. Chem. A* 1 (2013) 7816–7824.
- [23] X. Fan, Z. Xing, Z. Shu, L. Zhang, L. Wang, J. Shi, Improved photocatalytic activity of g-C₃N₄ derived from cyanamide-urea solution, *RSC Adv.* 5 (2015) 8323–8328.
- [24] F. Dong, Z. Ni, P. Li, Z. Wu, A general method for type I and type II g-C₃N₄/g-C₃N₄ metal-free isotype heterostructures with enhanced visible light photocatalysis, *New J. Chem.* 39 (2015) 4737–4744.
- [25] F. Dong, Z. Zhao, T. Xiong, Z. Ni, W. Zhang, Y. Sun, W.K. Ho, In situ construction of g-C₃N₄/g-C₃N₄ metal-free heterojunction for enhanced visible-light photocatalysis, *ACS Appl. Mater. Interfaces* 5 (2013) 11392–11401.
- [26] J. Xu, L. Zhang, R. Shi, Y. Zhu, Chemical exfoliation of graphitic carbon nitride for efficient heterogeneous photocatalysis, *J. Mater. Chem. A* 1 (2013) 14766–14772.
- [27] H. Yu, R. Shi, Y. Zhao, T. Bian, Y. Zhao, C. Zhou, G.I.N. Waterhouse, L.-Z. Wu, C.-H. Tung, T. Zhang, Alkali-assisted synthesis of nitrogen deficient graphitic carbon nitride with tunable band structures for efficient visible-light-driven hydrogen evolution, *Adv. Mater.* 29 (2017) 1605148-n/a.
- [28] G. Zhang, J. Zhang, M. Zhang, X. Wang, Polycondensation of thiourea into carbon nitride semiconductors as visible light photocatalysts, *J. Mater. Chem.* 22 (2012) 8083.
- [29] Z. Tong, D. Yang, Y. Sun, Y. Nan, Z. Jiang, Tubular g-C₃N₄ isotype heterojunction: enhanced visible-light photocatalytic activity through cooperative manipulation of oriented electron and hole transfer, *Small* 12 (2016) 4093–4101.
- [30] P. Niu, G. Liu, H.-M. Cheng, Nitrogen vacancy-promoted photocatalytic activity of graphitic carbon nitride, *J. Phys. Chem. C* 116 (2012) 11013–11018.
- [31] J. Ding, W. Xu, H. Wan, D. Yuan, C. Chen, L. Wang, G. Guan, W.-L. Dai, Nitrogen vacancy engineered graphitic C₃N₄-based polymers for photocatalytic oxidation of aromatic alcohols to aldehydes, *Appl. Catal. B: Environ.* 221 (2018) 626–634.
- [32] X. Wang, J. Cheng, H. Yu, J. Yu, A facile hydrothermal synthesis of carbon dots modified g-C₃N₄ for enhanced photocatalytic H₂-evolution performance, *Dalton Trans.* 46 (2017) 6417–6424.
- [33] M. Wu, J.M. Yan, X.N. Tang, M. Zhao, Q. Jiang, Synthesis of potassium-modified graphitic carbon nitride with high photocatalytic activity for hydrogen evolution, *ChemSusChem* 7 (2014) 2654–2658.
- [34] Y. Li, H. Zhang, P. Liu, D. Wang, Y. Li, H. Zhao, Cross-linked g-C₃N₄/rGO nanocomposites with tunable band structure and enhanced visible light photocatalytic activity, *Small* 9 (2013) 3336–3344.
- [35] Z. Lou, M. Fujitsuka, T. Majima, Pt-Au triangular nanoprisms with strong dipole plasmon resonance for hydrogen generation studied by single-particle spectroscopy, *ACS Nano* 10 (2016) 6299–6305.
- [36] Z. Zheng, T. Tachikawa, T. Majima, Single-particle study of Pt-modified Au nanorods for plasmon-enhanced hydrogen generation in visible to near-infrared region, *J. Am. Chem. Soc.* 136 (2014) 6870–6873.
- [37] Y. Li, R. Jin, Y. Xing, J. Li, S. Song, X. Liu, M. Li, R. Jin, Macroscopic foam-like holey ultrathin g-C₃N₄ nanosheets for drastic improvement of visible-light photocatalytic activity, *Adv. Energy Mater.* 6 (2016) 1601273.
- [38] P. Zhang, M. Fujitsuka, T. Majima, Hot electron-driven hydrogen evolution using anisotropic gold nanostructure assembled monolayer MoS₂, *Nanoscale* 9 (2017) 1520–1526.
- [39] Z. Bian, T. Tachikawa, P. Zhang, M. Fujitsuka, T. Majima, Au/TiO₂ superstructure-based plasmonic photocatalysts exhibiting efficient charge separation and unprecedented activity, *J. Am. Chem. Soc.* 136 (2014) 458–465.
- [40] I. Grigioni, K.G. Stamplecoskie, E. Selli, P.V. Kamat, Dynamics of photogenerated charge carriers in WO₃/BiVO₄ heterojunction photoanodes, *J. Phys. Chem. C* 119 (2015) 20792–20800.
- [41] Q. Liu, Q. Shang, A. Khalil, Q. Fang, S. Chen, Q. He, T. Xiang, D. Liu, Q. Zhang, Y. Luo, L. Song, In situ integration of a metallic 1T-MoS₂/CdS heterostructure as a means to promote visible-light-driven photocatalytic hydrogen evolution, *ChemCatChem* 8 (2016) 2614–2619.
- [42] R. Godin, Y. Wang, M.A. Zwiernburg, J. Tang, J.R. Durrant, Time-resolved

- spectroscopic investigation of charge trapping in carbon nitrides photocatalysts for hydrogen generation, *J. Am. Chem. Soc.* 139 (2017) 5216–5224.
- [43] V.W. Lau, I. Moudrakovski, T. Botari, S. Weinberger, M.B. Mesch, V. Duppel, J. Senker, V. Blum, B.V. Lotsch, Rational design of carbon nitride photocatalysts by identification of cyanamide defects as catalytically relevant sites, *Nat. Commun.* 7 (2016) 12165.
- [44] L. Shi, L. Yang, W. Zhou, Y. Liu, L. Yin, X. Hai, H. Song, J. Ye, Photoassisted construction of holey defective g-C₃N₄ photocatalysts for efficient visible-light-driven H₂O₂ production, *Small* 14 (2018) 1703142.
- [45] W. Tu, Y. Xu, J. Wang, B. Zhang, T. Zhou, S. Yin, S. Wu, C. Li, Y. Huang, Y. Zhou, Z. Zou, J. Robertson, M. Kraft, R. Xu, Investigating the role of tunable nitrogen vacancies in graphitic carbon nitride nanosheets for efficient visible-light-driven H₂ evolution and CO₂ reduction, *ACS Sustain. Chem. Eng.* 5 (2017) 7260–7268.